Investigation of Polarimetric Decomposition for Arctic Summer Sea Ice Classification Using Gaofen-3 Fully Polarimetric SAR Data

Lian He, Xiyi He, Fengming Hui, Yufang Ye, Tianyu Zhang, and Xiao Cheng

***Abstract*—The aim of this article was to investigate the potential of polarimetric decomposition of Chinese Gaofen-3 (GF-3) C-band fully polarimetric synthetic aperture radar (PolSAR) data for Arctic sea ice classification during summer season. Five different polarimetric decomposition approaches, including the Cloude-Pottier decomposition (Cloude), the Freeman three-component decomposition (Freeman3), the Freeman three-component decomposition using the extended Bragg model (Freeman3X), the Yamaguchi three-component decomposition (Yamaguchi3), and the nonnegative eigenvalue decomposition (NNED) were analyzed using 35 scenes of GF-3 PolSAR data collected over the Fram Strait, Arctic from June 14–18, 2017. Polarimetric features extracted from these five methods were evaluated and utilized to train random forest classifiers to classify open water (calm water and rough water) and sea ice types (melted ice, unmelted ice, and deformed ice). The results show that NNED could ensure physically valid decomposed powers while the other three model-based decompositions had negative values. In terms of sea ice classification, NNED had the highest feature importance scores and achieved an overall accuracy and Kappa coefficient of about 86.18% and 0.82, respectively. Inclusion of radar incidence angle as a feature in the classifier could slightly improve the classification accuracy by about 3%. The influence of incidence angle on sea ice classification accuracy was also investigated and it was found that high incidence angles (39°–46°) were superior to low incidence angles (21°–27°) due to the overall higher accuracies.**

***Index Terms*—Arctic sea ice, Gaofen-3, polarimetric decomposition, polarimetric synthetic aperture radar, random forest.**

I. Introduction

SEA ice in both polar regions is an integral part of the climate system. During the past four decades, rapid and dramatic declines in extent, age and thickness in Arctic sea ice conditions have been observed [1]. Furthermore, the duration of the Arctic sea ice melt season has been observed to become longer [2], i.e., the ice is starting to melt earlier in the year and freeze later than it used to. While snow-covered and bare sea ice has a large surface albedo, melted snow cover or sea ice tends to absorb more of solar energy due to decreased surface albedo, which plays a key role in the decline of sea ice in the Arctic through the ice-albedo feedback mechanism [3]. Therefore, summer sea ice monitoring is highly required for many activities, including ship navigation and OFF-shore operations, and in various scientific studies [4].

Synthetic aperture radar (SAR) has all-weather and all-time imaging capability, and can provide undisturbed observation of sea ice regardless of cloud coverage or darkness in polar regions with a high spatial resolution. SAR has been extensively applied to sea ice classification using a variety of approaches [5]–[10]. However, single- or dual-polarization backscattering coefficients have limited ability to discriminate certain sea ice types and open water states [11], [12]. The use of only the backscatter values in the classification algorithm also limits the number of distinguished sea ice types [13]. Therefore, additional information such as polarimetric characteristics [14], [15] and image texture features [16] were introduced to improve sea ice classification.

Fully polarimetric SAR (PolSAR) data provide, for each pixel, the full complex scattering matrix, including amplitude and phase information of the four transmit–receive channels (HH, HV, VH, and VV). This contains a wealth of information on the target properties, such as size, shape, orientation, and dielectric constant, and has been widely used for geophysical parameter estimation, such as soil moisture [17]–[19] and sea ice parameters [20]–[22]. In terms of sea ice classification, polarimetric decomposition of PolSAR data is beneficial in extracting polarimetric features, which provide different information from backscattering coefficients. Polarimetric decomposition parameters are helpful in interpreting different types of sea ice through scattering mechanisms, and thus, provide a more theoretical basis for sea ice classification [22]–[27]. A considerable amount of research has examined the application of polarimetric decomposition methods in sea ice classification during the winter and fall seasons [22]–[30]. However, only a few of studies concentrate on the melt period [31]–[37] and summer sea ice classification still needs further assessment.

Manuscript received January 20, 2022; revised February 17, 2022 and April 4, 2022; accepted April 22, 2022. Date of publication April 27, 2022; date of current version May 25, 2022. This work was supported in part by the National Key R&D Program of China under Grant 2019YFC1509104, in part by the Innovation Group Project of Southern Marine Science and Engineering Guangdong Laboratory (Zhuhai) under Grant 311021008, and in part by the Science and Technology Projects in Guangzhou under Grant 202102020525. *(Corresponding author: Xiao Cheng.)*

Lian He, Xiyi He, Fengming Hui, Yufang Ye, and Xiao Cheng are with the School of Geospatial Engineering and Science, Sun Yat-sen University, Zhuhai 519082, China, and also with the Southern Marine Science and Engineering Guangdong Laboratory (Zhuhai), Zhuhai 519082, China (e-mail: helian_2006@126.com; hexy79@mail2.sysu.edu.cn; huifm@mail.sysu.edu.cn; yeyf8@mail.sysu.edu.cn; chengxiao9@mail.sysu.edu.cn).

Tianyu Zhang is with the State Key Laboratory of Remote Sensing Science, College of Global Change and Earth System Science, Beijing Normal University, Beijing 100875, China (e-mail: zhangty@mail.bnu.edu.cn).

Digital Object Identifier 10.1109/JSTARS.2022.3170732

Among the polarimetric decomposition methods tested for extracting polarimetric parameters in sea ice classification, there are two main approaches, i.e., the eigenvalue-based decomposition approaches and the model-based decomposition approaches, pioneered by Cloude and Pottier [38] and Freeman and Durden [8], respectively. The model-based decomposition techniques are popularly used due to the easy physical interpretation and their simplicity. Within the framework of the Freeman-Durden decomposition [8], efforts have been made to solve some existed issues, including the occurrence of negative powers [39], [40], zero cross-polarization in surface scattering component [17], and new scattering model for manmade targets [41], [42]. Yamaguchi *et al.* [43] introduced a variety of volume scattering models to account for the orientation effects of the dipoles forming the volume. Van Zyl *et al.* [39] proposed a nonnegative eigenvalue decomposition to ensure valid decomposed powers. Hajnsek *et al.* [18] extended the Bragg surface model to the X-Bragg surface model to account for the cross-polarization term induced by the depolarization effect. To our knowledge, these advanced polarimetric decomposition methods has not yet been investigated for sea ice classification.

Gaofen-3 (GF-3) is the first Chinese multipolarization and high resolution C-band SAR satellite and has fully polarimetric capability. The measured backscattering coefficients from GF-3 PolSAR has been tested for sea ice classification using a deep convolutional neural network [44]. In addition, polarimetric decomposition of GF-3 PolSAR data has demonstrated great potential in applications such as land cover classification [45] and soil moisture estimation [46]. However, polarimetric decomposition of GF-3 PolSAR data for sea ice classification has not been evaluated.

The objective of this article is to test the capabilities of polarimetric decomposition of GF-3 PolSAR data for sea ice classification during the summer season. Five representative polarimetric decomposition models, including the Cloude-Pottier decomposition [38] (referred to as Cloude), the Freeman three-component decomposition [47] (referred to as Freeman3), the Freeman three-component decomposition using extended Bragg surface scattering model [18] (referred to as Freeman3X), the Yamaguchi three-component decomposition [43] (referred to as Yamaguchi3), and the nonnegative eigenvalue decomposition [40] (referred to as NNED), were analyzed using Gaofen-3 fully polarimetric SAR data collected over the Fram Strait, Arctic from June 14–18, 2017. Polarimetric features extracted from different decompositions were evaluated and fed into random forest classifiers for sea ice classification with the accuracy assessed. The influences of radar incidence angle on polarimetric decomposition features and classification accuracy were also investigated.

II. Study Area and Datasets

A. Study Area

The Fram Strait is located between Svalbard and the East Greenland coast and is the main gate for sea ice export from the Arctic Ocean. It has been estimated that about 10% of the Arctic sea ice cover is exported through Fram Strait every year [48]. Therefore, the Fram Strait plays an important role in the sea ice mass balance of the Arctic. The sea ice cover in this region is highly variable in space and time as it is exposed to sea ice drifts forced by the winds and ocean currents [49]. The study area is indicated in Fig. 1 by the solid red rectangle.

B. GF-3 PolSAR Data

GF-3 is the first Chinese high-resolution SAR satellite to acquire multipolarized SAR image at meter-level resolution and was launched in August 2016. The GF-3 satellite operates at C band (5.4 GHz) and is in a sun-synchronous dusk-dawn orbit at an altitude of 755 km with an inclination of 98.41° and a repeat cycle of orbit of about 29 days. The GF-3 satellite provides imaging in 12 different modes, including spotlight, stripmap, scan, and wave, with spatial resolutions varying from 1 to 500 m and swath widths ranging from 10 to 650 km. Among the 12 modes, three imaging modes, the Quad Polarization Stripmap I (QPSI), the QPS II (QPSII), the wave mode, have fully polarimetric capability with a resolution up to 8 m [50].

In this article, 35 scenes of GF-3 SAR data in QPSII mode were collected during the period of June 14–18, 2017 over the Fram Strait and are listed in Table I. The QPSII mode has a swath width of 40 km with a nominal spatial resolution of about 25 m (by applying a multilook factor of about 3 in range and 2 in azimuth) and an alternate incidence angle ranging from 20° to 50°. For the QPSII mode, GF-3 provides 32 beams, which are coded from 217–232 and 473–488 for the right and left look directions [51]. Each beam has different incidence angles. For sea ice classification, the 35 SAR images were split into training and validation sets, with the number being 22 and 13, respectively. The location of the training and validation images is displayed in Fig. 1.

The processing level of the collected data is Level 1A single look complex (SLC), which contains the amplitude and phase information. For the GF-3 SLC data, the quantitative constants in the metafile of each image product are used to quantify each polarization channel data first. Radiometric and polarimetric calibrated image for each polarized channel S_{qp} can be obtained by [52]

$$S_{pq} = \frac{Q_v}{32767} \cdot 10^{(-K_{dB}/20)} \cdot (I_{pq} + i \cdot Q_{pq}) \tag{1}$$

where Q_{v} and K_{dB} are calibration coefficients obtained from the metafile; the subscripts p and q refer to the polarization state (H or V) of the incident and scattered fields, respectively; I and Q represent the real and imaginary parts of the SAR image data, respectively; i stands for the imaginary unit.

GF-3 has been demonstrated to have a similar polarimetric performance to RADARSAT-2 using scattering properties and corner reflectors [52]–[55]. After calibration, the scattering matrix was transformed into a coherency matrix (by applying a multilook factor of about 3 in range and 2 in azimuth), resulting a spatial resolution of about 25 m. Speckle noise in the SAR data was reduced using the refined Lee filter with a window size of 3×3 [56], which could preserve polarimetric information in homogeneous areas.

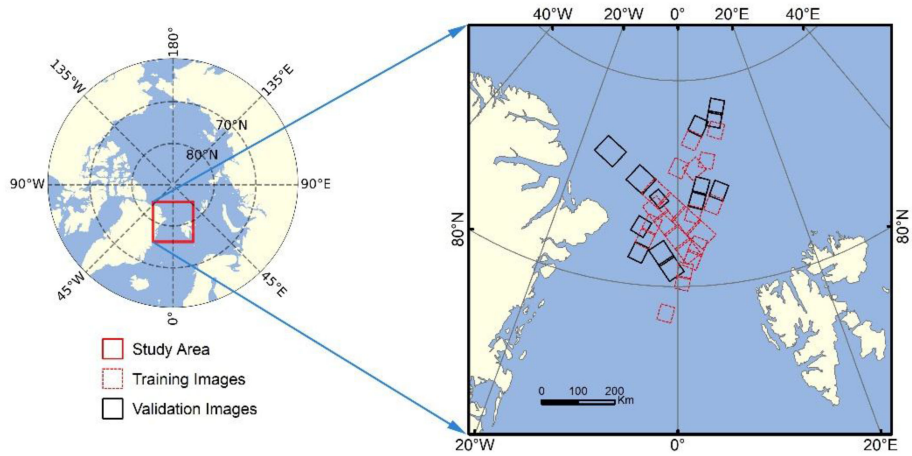

Fig. 1. Map of the study area of Fram Strait, showing the location of the satellite scenes. The red dashed rectangles display the training samples while the black boxes display the validation samples.

TABLE I
LIST OF GF-3 FULLY POLARIMETRIC SAR DATA USED IN THIS ARTICLE

Beam Code	Acquisition date	Orbit	Incidence angle (°)	Number of training images	Number of validation images
217	2017-6-16	Ascending	19.1 – 23.2	4	2
218	2017-6-17	Descending	22.6 – 25.7	1	1
219	2017-6-15, 2017-6-17	Ascending	25.3 – 28.6	4	2
226	2017-6-14, 2017-6-15	Descending	37.9 – 40.2	3	2
228	2017-6-17	Descending	41.7 – 43.8	4	2
230	2017-6-18	Descending	44.9 – 46.8	3	2
232	2017-6-16	Descending	47.7 – 49.4	3	2

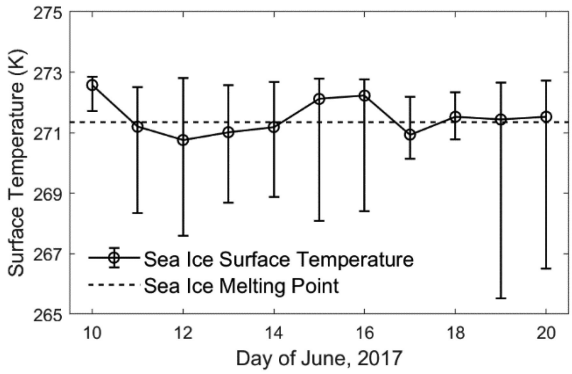

Fig. 2. Daily median values of sea ice surface temperature of the study area from MODIS/Terra sea ice and ice surface temperature product for the period of June 10–20, 2017. The upper and lower bounds indicate the 90th and 10th percentile of all the sea ice surface temperature values, respectively.

In order to investigate the surface temperature and melting condition of sea ice in the study area, the MODIS/Terra sea ice and ice surface temperature product (Product ID: MOD29P1D, Version 61) [57] was utilized. This product provides daily daytime sea ice extent and ice surface temperature (IST) at a spatial resolution of 1 km. Sea ice is detected using the normalized difference snow index and ice surface temperature is estimated using the split-window technique [58]. Fig. 2 shows the temporal dynamics of sea ice surface temperature over the study area from June 10–20, 2017. The melting temperature of sea ice is about 271.35 K (−1.8 °C). It was shown that the median values of IST fluctuated around the melting point, indicating that a large part of the sea ice in the study area had IST above the melting point and began to melt during the acquisition period of GF-3 data. The upper bounds of IST were close to 273 K and appeared more stable than the lower limits.

III. METHODOLOGY

A. Polarimetric Decomposition Methods

Polarimetric decomposition allows interpretation of the measured PolSAR data by separating it into basic scattering mechanisms. Several polarimetric decomposition approaches have been proposed for extracting polarimetric features in remote sensing image classification. In this article, five models were analyzed, including one eigenvalue-based and four model-based decomposition methods.

The eigenvalue-based decomposition method proposed by Cloude and Pottier [38] (referred as to Cloude) is a mathematical technique, in which the measured coherency matrix is represented in terms of its eigenvalues and eigenvectors. Three polarimetric features (the entropy H, the anisotropy A, and the mean scattering angle α) related to the eigenvalues and

TABLE II
MODEL-BASED POLARIMETRIC DECOMPOSITIONS TESTED IN THIS ARTICLE

Polarimetric decomposition methods	Surface scattering model	Double-bounce scattering model	Volume scattering model	Determination of volume intensity	Reference
Freeman3	Bragg	Fresnel	Random volume model	Directly derived	Freeman and Durden [47]
Freeman3X	X-Bragg	Fresnel	Random volume model	Directly derived	Hajnsek *et al.* [18]
Yamaguchi3	Bragg	Fresnel	Yamaguchi volume model	Directly derived	Yamaguchi *et al.* [43]
NNED	Bragg	Fresnel	Random volume model	Nonnegative eigenvalue constrained	Van Zyl *et al.* [40]

*Freeman3 represents for Freeman three-component decomposition; Freeman3X represents for Freeman three-component decomposition using extended Bragg model; Yamaguchi3 stands for Yamaguchi three-component decomposition; NNED indicates nonnegative eigenvalue decomposition.

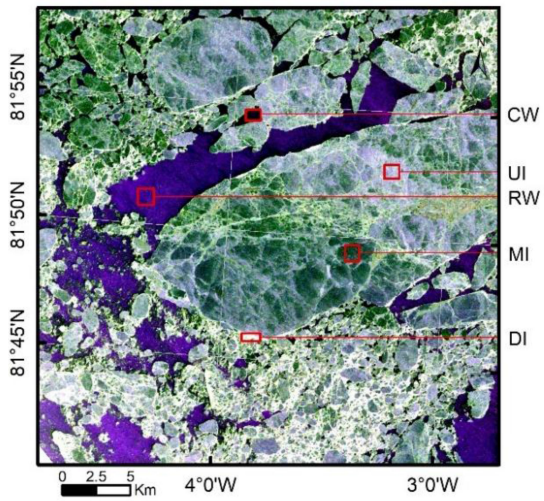

Fig. 3. RGB image of the Pauli decomposition powers (in decibels) of one training image acquired on June 17, 2017 (Red: $|S_{\rm hh} - S_{\rm vv}|^2$; Green: $2|S_{\rm vh}|^2$; Blue: $|S_{\rm hh} + S_{\rm vv}|^2$). The incidence angle was about 27°. Different sea surface types were identified, namely DI, UI, MI, RW, and CW.

eigenvectors are developed to interpret the scattering mechanisms of the target.

The model-based polarimetric decomposition is physically based and separates the measured coherency (or covariance) matrix into a combination of a few simple components, which are then linked to physical scattering mechanisms. In this article, four model-based decompositions, namely, Freeman3 [47], Freeman3X [18], Yamaguchi3 [43], and NNED [40], were utilized and their characterizations are summarized in Table II. With these four models, decomposed powers of surface scattering $P_{\rm s}$, double-bounce scattering $P_{\rm d}$, and volume scattering $P_{\rm d}$ can be extracted and used for sea ice classification.

B. Sea Ice Classification

1) Training and Validation Sample Selection: The sea ice types are usually classified into multiyear ice, first-year ice, new ice or lead, and open water (OW) during wintertime. However, during the summer season, the number of types that could be classified significantly reduces due to melting conditions [59]. In this article, five sea surface types were identified in the study area, namely calm water (CW), rough water (RW), melted ice (MI), unmelted ice (UI), and deformed ice (DI). As an example, Fig. 3 indicates the visual interpretation of different types. An OW class roughened by winds and having relatively high backscattering coefficients was defined as RW while an OW class having smooth surface and low backscatters was identified as CW. Both MI and UI were chosen as ice floes while MI appears dark due to melting conditions and UI appears bright. DI consisted of brash ices, ice ridges, and floe edges.

In this article, 35 images acquired with different antenna beams having different incidence angles were collected and are listed in Table I. Among them, 22 images were assigned for training, and the remaining 13 images were used for validation. All the training and validation samples were selected by visual interpretation, with the number of pixels being about 1.3 million and 1.0 million, respectively.

2) Random Forest Classifier: In this article, the random forest (RF) classifier was utilized for sea ice classification. The RF is an ensemble learning method for classification. It, first, constructs a number of decision tree classifiers on various subsamples of the dataset, and then uses averaging to improve the predictive accuracy and control overfitting [60]. The RF can handle large datasets, especially in high-dimensioned feature spaces and has been widely used for remote sensing image classification [61].

There are three hyperparameters in the RF classifier needed to be tuned, i.e., the number of trees (NT), the maximum depth of the tree (ND), and the maximum number of features (NF) to consider when looking for the best split in each node. In general, larger values of NT and ND are expected to yield models to better fit the data, but it will take more time to train the model and can cause overfitting. In this article, the value of NF was set as the square root of the number of input features, as suggested for classification tasks [60]. Therefore, only two hyperparameters (i.e., NT and ND) are needed to be tuned. To determine the best values of NT and ND, a grid search with five-fold cross validation was used. The value of NT was set on a logarithmic scale with values being (1, 2, 4, 8, 16, 32, 64), and the ND increased from 2 to 20 with an interval of 2. The optimal values for NT and ND are selected based on the saturation of score increments according to grid search results [9]. The RF model was implemented through the Python Scikit-Learn [62].

In order to evaluate the classification performance, the confusion matrix [63] was first computed based on the validation dataset. From the confusion matrix, two statistical parameters, i.e., overall accuracy (OA) and Kappa coefficient, were calculated. OA is defined as the ratio of correctly classified pixels to the total number of pixels. Kappa coefficient reflects a measure of the difference between actual agreement and chance agreement in the classification [64].

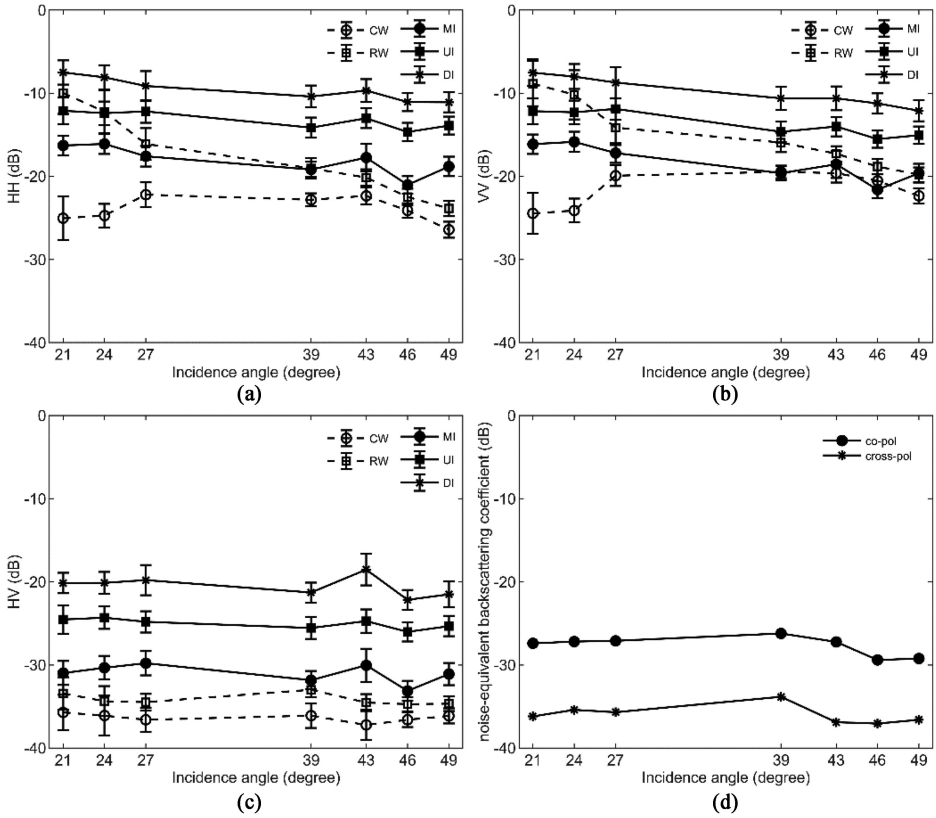

Fig. 4. (a)–(c) Display mean backscattering coefficient values of training samples with one standard deviation versus incidence angle for HH, VV, and HV polarizations, respectively. (d) Indicates the estimated noise-equivalent backscattering coefficient for copolarizations (HH and VV) and cross polarizations (HV and VH) at different incidence angles. Noise level is calculated using the training samples of open water.

IV. Results and Discussion

A. Backscattering Coefficient of Different Sea Surface Types

The incidence angle dependencies of radar backscattering coefficients for different sea ice types have been extensively studied [65]–[67] and the effect of incidence angle on radar backscatter and texture features should be considered for sea ice classification [68], [69]. Fig. 4 shows scatter plots of radar backscattering at three polarizations (HH, VV, and HV) versus incidence angle for five different sea surface types using the training samples extracted from training images in Table I. In general, the copolarized backscatters of all sea ice types decrease as the incidence angle increases except for calm water. The three ice types (DI, UI, and MI) have comparable sensitivity to the incidence angle, with values of about -0.11 dB/1° and –0.15 dB/1° for HH and VV, respectively. RW shows the highest sensitivity to the incidence angle (–0.45 dB/1° for HH and –0.36 dB/1° for VV), while CW has the lowest sensitivity. The lack of incidence angle dependency for CW might be attributed to the variation in surface roughness since the samples were extracted from different images. For cross polarization, the dependence of the radar backscatter on the incidence angle has reduced significantly, which agrees well with the results from [27], [70].

In terms of sea ice classification, it can be observed that HV polarization can distinguish certain classes quite distinctively while HH and VV polarizations are not very discriminative. DI and UI can be easily separated from the other types using HV backscatter at each incidence angle. RW has a large backscatter range at HH and VV polarizations making it difficult to discriminate RW from sea ice types (DI, UI, and MI), which is consistent with observations in [68].

It has been pointed out that the noise-equivalent backscattering coefficients (NEBC) of each polarization is very important [67], [71] for analyzing the incidence angle dependencies. In order to investigate the influence of noise floor, the method proposed in [72] was utilized to estimate the noise-equivalent backscattering coefficients. Training samples from the open water class were used to estimate the noise levels. Fig. 4(d) demonstrates the estimated averaged NEBC values for cross- and copolarizations at different incidence angles. The NEBC values of cross polarization for the incidence angles of 21° (beam code 217 in Table I) and 27° (beam code 219 in Table I) were about –35.5 dB, which is very close to the result from the recent study in [51]. It can be seen that backscattering coefficients of CW were very close to the noise levels at all incidence angles, which may be the anther reason that CW showed less sensitivity to the incidence angle.

B. Comparison of Different Polarimetric Decomposition Methods

1) Eigenvalue-Based Decomposition: Fig. 5 shows the mean values and standard deviation of the alpha angle α, the entropy H,

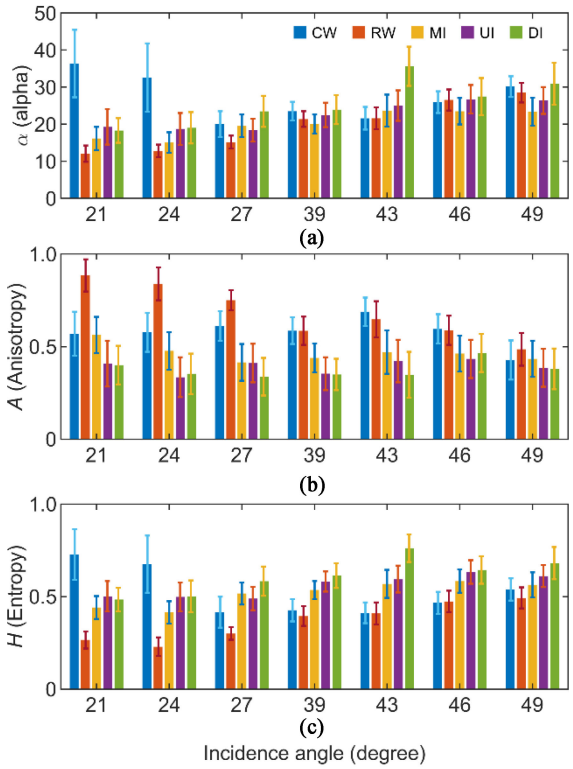

Fig. 5. Mean values and associated standard deviation (error bars) of (a) alpha angle α, (b) anisotropy A, and (c) entropy H for five sea surface types at different incidence angles from training samples.

and the anisotropy A for five sea surface types at seven different incidence angles from the training samples. It was found that all surface types had scattering angles below 40°, indicating the dominance of surface scattering according to [38]. Results showed high entropy for DI, followed by UI and MI at almost all incidence angles, while open water (both CW and RW) had low entropy except for CW at low incidence angles (21° and 24°) where high α and H values were observed. The observed elevated α and H values of calm water at 21° and 24° may be caused by the relatively low backscattering coefficients, which are near the system noise levels (as indicated in Fig. 4). In this case, the obtained polarimetric parameters may not be reliable [71]. Therefore, it is necessary to consider effects of the system's noise level as pointed out by [25].

All three parameters, α, H, and A, demonstrated certain incidence angle dependencies for each sea surface type (excluding CW). There was a clear upward trend in mean α and H while a slight downward trend in mean A value was observed as the incidence angle increased. Meanwhile, the strength of sensitivity to the incidence angle varies with parameter and sea surface type. For example, DI displays higher sensitivities to the incidence angle for α and H, and less sensitivity for A. However, RW has a high sensitivity for all three parameters.

In terms of classification, results demonstrated the capability of H to separate between RW and sea ice (MI, UI, DI) except for high incidence angles of 46° and 49°. However, MI, UI, and DI were mixed. The parameter A also showed the potential to discriminate RW and sea ice at low incidence angles.

2) Model-Based Decompositions: Fig. 6 displays the incidence angle dependences of decomposed powers from training samples using the four model-based decomposition methods, namely, Freeman3, Freeman3X, Yamaguchi3, and NNED (see Section II). Five sea surface types were analyzed, i.e., CW, RW, MI, UI, and DI. Note that all powers were normalized to the total power (i.e., surface + double-bounce + volume), therefore highlighting the relative strength between the three components.

For the five sea surface types, the surface scattering was always dominant, generally taking over 60% of the total power. Meanwhile, the double-bounce scattering counted for only about 7% of the total power and appeared stable among different sea surface types. These results are consistent with the findings in winter sea ice [25], [27]. The decomposed powers for various sea surface types (open water, melted ice, unmelted ice, and deformed ice) showed a gradual decrease in surface scattering and an overall increase in volume scattering, which agrees well with observations in [27].

All the relative decomposed powers (P_s, P_d, and P_v) showed clear incidence angle dependencies for each sea surface type (excluding CW). A decreasing surface component was observed with increasing incidence angle, as expected. The same trend was also observed in the decomposed surface component (in power unit). For the relative decomposed double bounce and volume powers, an overall upward trend was observed. However, it should be noted that for those two decomposed components in power unit, they decreased as the incidence angle increased.

Different decomposition approaches yielded quite different results. The Freeman3 provided the highest relative volume component since the volume scattering contribution is solely determined by the cross-polarization term by using $P_v = 4 * T_{33}$ (T_{33} is the element of the measured coherency matrix, which is a 3×3 complex Hermitian matrix) [47]. The introduce of X-Bragg model in Freeman3X could help to slightly reduce the volume scattering and increase the surface scattering when compared to Freeman3, since it could consider the cross-polarized scattering caused by surface roughness. The Yamaguchi3 provided three volume scattering models, i.e., horizontally, vertically, and randomly oriented dipoles, to be chosen according to the VV/HH power ratio. It had a much lower volume component than Freeman3, which can be explained by that the volume component is determined by $P_v = 15/4 * T_{33}$ if vertical or horizontal volume model is chose [18].

It can be concluded that that while Freeman3 and FreemanX tend to overestimate the volume scattering power, Yamaguchi3 and NNED could generate more reasonable results. For example, for DI at incidence angle 43° (as indicated in Fig. 6), the relative volume component almost reaches to above 50%, which does not agree with the results from the Cloude decomposition (see Fig. 5) and other studies [27], [28] that the surface scattering is always dominant.

It should be noted that about 1% of the pixels had negative surface or double-bounce components in Freeman3 and Freeman3X, and the number of pixels with negative powers significantly reduced to about 0.3% in Yamaguchi3. NNED used nonnegative eigenvalues to constrain the volume scattering component and had the lowest volume scattering component.

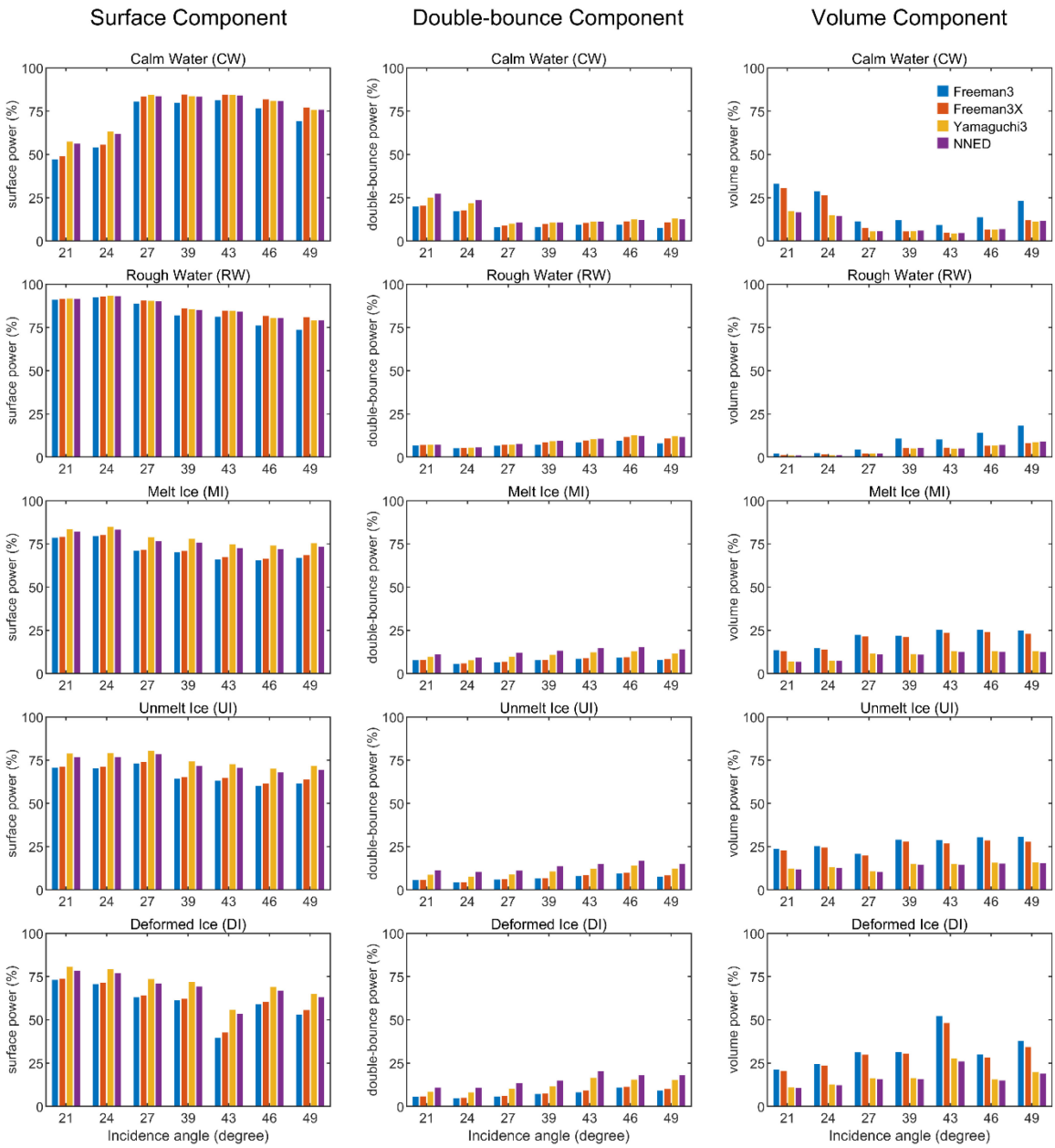

Fig. 6. Incidence angle dependence of relative decomposed powers: surface (left column), double-bounce (middle column), and volume (right column) scattering for five different sea ice types (top to bottom) from training samples.

Therefore, NNED could ensure physically valid decomposed powers and performed the best.

C. Feature Importance Evaluation

In order to quantitatively analyze the contribution of each polarimetric features for sea ice classification, 15 features extracted from the five decomposition methods were fed into random forest classifier and the importance of each feature could be computed. Fig. 7 displays the importance of 15 features. All the importance values are positive and sum to 1.0. The higher the value, the more important is the contribution of the matching feature to the prediction function.

In terms of comparison among different polarimetric decomposition methods, the total feature importance of each algorithm was calculated and results show that model-based decompositions (i.e., Freeman3, Freeman3X, Yamaguchi3, and NNED) had much higher importance values than that of the eigenvalue-based decomposition (Cloude). NNED had the highest total importance value of 0.344, followed by the Yamaguchi3 and FreemanX (0.231 and 0.204), and then the Freeman3 decomposition (0.166). Cloude had the lowest total importance of 0.055, indicating that the Cloude decomposition do not contain very much discrimination information, which is consistent with the results in Fig. 5 and the findings in [25].

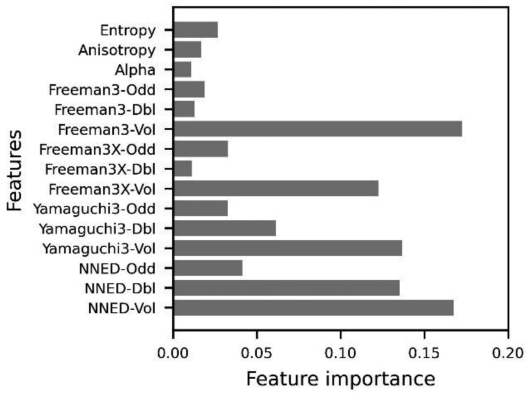

Fig. 7. Feature importance obtained using random forest from training samples. Odd, Dbl, and Vol indicate surface scattering, double-bounce scattering, and volume scattering, respectively.

TABLE III
CLASSIFICATION ACCURACY OF DIFFERENT FEATURE COMBINATIONS

Classification features*	OA (%)	Kappa
$\sigma^0_{\rm HH}$, $\sigma^0_{\rm VV}$, $\sigma^0_{\rm HV}$	87.03	0.83
H, A, α	63.00	0.50
$P_{\rm s}$, $P_{\rm d}$, $P_{\rm v}$	86.18	0.82
$\sigma^0_{\rm HH}$, $\sigma^0_{\rm VV}$, $\sigma^0_{\rm HV}$, θ	89.93	0.87
H, A, α, θ	65.26	0.53
$P_{\rm s}$, $P_{\rm d}$, $P_{\rm v}$, θ	89.08	0.85
$P_{\rm s}$, $P_{\rm d}$, $P_{\rm v}$, H, A, α, θ	89.39	0.86
$\sigma^0_{\rm HH}$, $\sigma^0_{\rm VV}$, $\sigma^0_{\rm HV}$, $P_{\rm s}$, $P_{\rm d}$, $P_{\rm v}$, θ	89.99	0.87

* $\left(\sigma^0_{\rm HH}, \sigma^0_{\rm VV}, \sigma^0_{\rm HV}\right)$ are backscatter coefficients; H, A, and α are entropy, anisotropy, and alpha angle from Cloude decomposition; $P_{\rm s}$, $P_{\rm d}$, $P_{\rm v}$ are suface, double-bounce and volume scattering power obtained from NNED; θ indicates the radar incidence angle.

Among the three scattering components of the model-based decomposition methods, the volume component always had the highest importance value although the volume component is not dominant (as indicated in Fig. 6). This might be explained by the fact that the volume component is mainly determined by the cross-polarization term, which has the largest discrimination capability, as indicated for HV in Fig. 4. The importance of double bounce and surface components varied for different model-based decomposition approaches. While Yamaguchi3 and NNED had larger importance values in double-bounce component, Freeman3 and Freeman3X had higher importance values in surface component. Reasonable estimation of volume scattering in NNED and Yamaguchi3 enhances the discrimination capability of nondominant scattering components, highlighting the importance of correct volume scattering removal of decomposition methods.

Due to the nonnegative decomposed power and its high feature importance values, NNED will be used for sea ice classification. In addition, although the Cloude decomposition had relatively low feature importance, it will also be tested in sea ice classification since it could provide quite different information from NNED.

D. Sea Ice Type Mapping and Validation

For sea ice classification, features from backscattering coefficients $\left(\sigma^0_{\rm HH}, \sigma^0_{\rm VV}, \sigma^0_{\rm HV}\right)$, NNED ($P_{\rm s}$, $P_{\rm d}$, $P_{\rm v}$), Cloude (H, A, α) as well as radar incidence angle θ were tested. Eight combinations of features were evaluated using

RF classifiers and the configurations of all experiments as well as their classification accuracies are listed in Table III. The optimal values for NT and ND were set as 12 and 32, respectively, which were selected based on the saturation of score increments [9].

The results indicate that features (H, A, α) from Cloude yielded the lowest classification accuracy, with OA and Kappa being 63% and 0.50, respectively. In contrast, backscatter coefficients $\left(\sigma^0_{\rm HH}, \sigma^0_{\rm VV}, \sigma^0_{\rm HV}\right)$ had the highest accuracy with OA and Kappa coefficient being 87.03% and 0.83, respectively. The use of features ($P_{\rm s}$, $P_{\rm d}$, $P_{\rm v}$) from NNED had OA and Kappa values of 86.18% and 0.82, respectively, indicating that the utilization of polarimetric decomposition features could achieve comparable classification accuracy to backscattering coefficients, which agrees with the finding in [25].

The inclusion of radar incidence angle θ as a feature in classification helped to improve the overall accuracy by about 3% for all three of the backscattering coefficients, Cloude and NNED. Therefore, it is recommended that the incidence angle should be considered for sea ice classification. The combination of features from different decomposition methods, i.e., Cloude + NNED, could slightly improve the classification accuracy compared to only using of NNED. Combination of backscattering coefficients and decomposed powers had the highest accuracy.

As a demonstration, the classification results of the SAR image acquired on June 15, 2017 are presented in Fig. 8. The SAR image had an incidence angle of about 27° and was covered different sea surface types. The results of the sea ice type maps are shown in Fig. 8(b)–(d), obtained from Cloude (H, A, α, θ), NNED ($P_{\rm s}$, $P_{\rm d}$, $P_{\rm v}$, θ), and backscattering coefficients $\left(\sigma^0_{\rm HH}, \sigma^0_{\rm VV}, \sigma^0_{\rm HV}, \theta\right)$, respectively. Features from Cloude have the capability to discriminate open water and sea ice. However, they demonstrate difficulties in separating different sea ice types. Sea ice maps from backscattering coefficients and NNED are very similar to each other and most of the pixels can be classified correctly. However, some DI could be classified as UI since the backscatters and polarimetric decomposition parameters from DI and UI can be similar.

In order to investigate the influence of the incidence angle on sea ice classification accuracy, Fig. 9 displays the overall accuracy and Kappa coefficient values for different incidence angles, which were acquired with different antenna beams. In general, the classification accuracy increases as the incidence angle increases from 21° to 46°. However, further increasing the incidence angle from 46° to 49° shows a decrease in classification accuracy. The previous study from [26] also demonstrated that a larger incidence angle (39°) provide better discrimination of different sea ice types compared with the smaller angle (29°). For the investigated data, high incidence angles (i.e., 39° to 46°) are superior to low incidence angles (i.e., 21° to 27°) due to the overall higher accuracies.

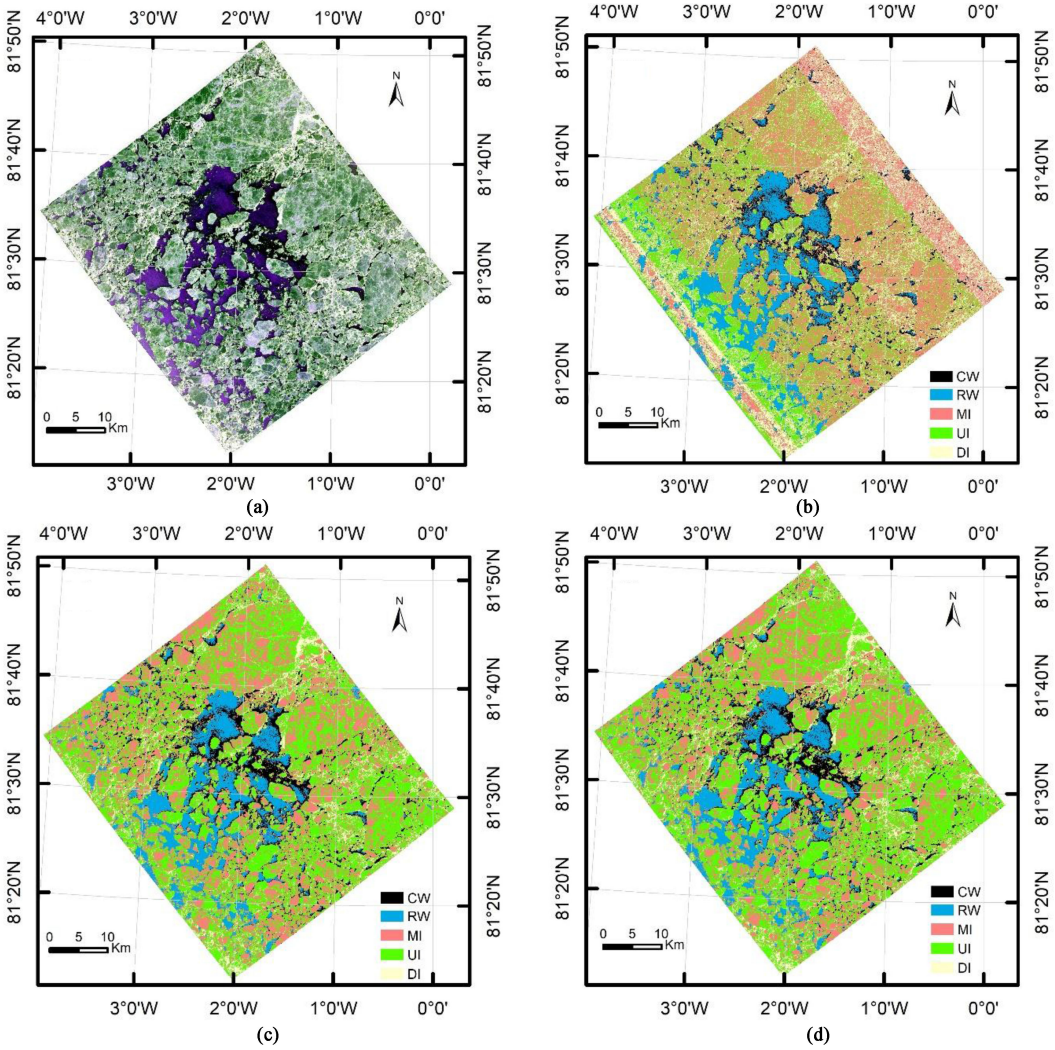

Fig. 8. Image maps of (a) original SAR image displayed in Pauli decomposition. (b) Classification map using Cloude decomposition with incidence angle. (c) Classification map using backscattering coefficients with incidence angle. (d) Classification maps using NNED with incidence angle.

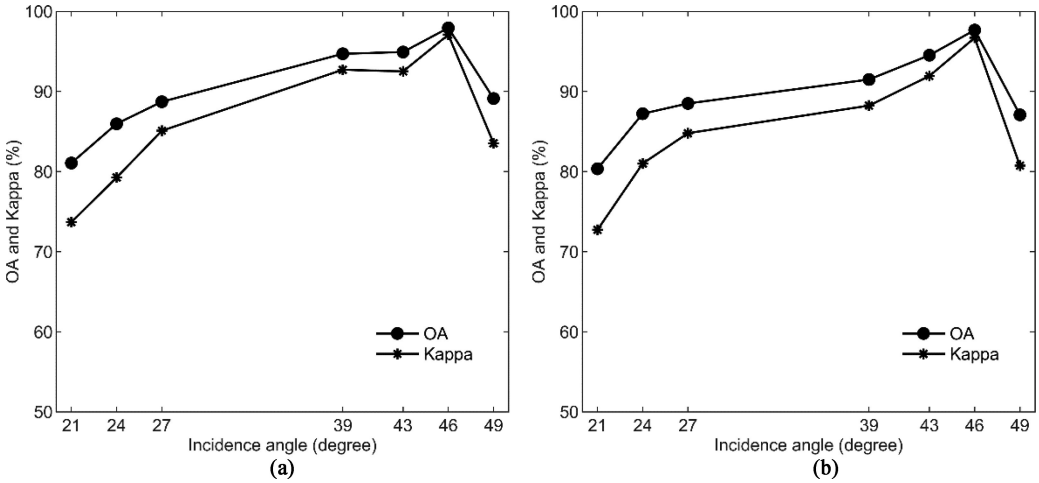

Fig. 9. Dependence of classification accuracy on incidence angle for (a) features $\left(\sigma^0_{\mathrm{HH}}, \sigma^0_{\mathrm{VV}}, \sigma^0_{\mathrm{HV}}\right)$ from backscatter coefficients and incidence angle and (b) features (P_{s}, P_{d}, P_{v}) from NNED and incidence angle. Classification accuracy parameters (OA and Kappa coefficient) were computed based on the validation dataset.

V. Conclusion

This article provided an extensive analysis of five different decomposition methods for parameter feature extraction in Arctic summer sea ice classification using Chinese GF-3 C-band fully polarimetric SAR (PolSAR) data. One eigenvalue-based decomposition (Cloude-Pottier decomposition) and four model-based decompositions, including the Freeman three-component decomposition, the Freeman three-component decomposition using the extended Bragg model, the Yamaguchi three-component decomposition, and the nonnegative eigenvalue decomposition, were tested. The extracted polarimetric parameters as well as backscattering coefficients were analyzed and utilized for sea ice classification with accuracy assessed.

The results indicated that the surface scattering dominated over summer sea ice. NNED could ensure physically valid decomposed powers while the other three model-based decompositions had negative values. Meanwhile, NNED had the highest feature importance scores in total while the Cloude decomposition had the lowest, indicating that NNED was more suitable for sea ice classification.

Different combinations of parameters were also evaluated using random forest classifiers. The results show that NNED has an OA and Kappa coefficient of about 86.18% and 0.82, respectively. Classification accuracy from NNED was very close to that from backscattering coefficients, which is in good agreement with previous findings. However, NNED could provide a better interpretation about the scattering mechanisms of sea ice. The inclusion of incidence angle as a feature can improve the classification accuracy, emphasizing the requirement for the incidence angle as a feature in sea ice classification using SAR data. Furthermore, the combination of NNED and backscattering coefficients could slightly increase the classification accuracy.

Since GF-3 PolSAR data were acquired using different antenna beams having different incidence angles (with the mean incidence angle being 21°, 24°, 27°, 39°, 43°, 46°, and 49°), the influence on classification accuracy was investigated and it was found that high incidence angles (39° to 46°) were superior to low incidence angles (21° to 27°) due to the overall higher accuracies, which can help to determine the optimal incidence angle for sea ice classification. However, due to the lack of data availability, only 7 discrete incidence angles were analyzed, making it important to further investigate these polarimetric decompositions for a comprehensive range of incidence angles in future studies.

This article confirms the capability of GF-3 PolSAR data for sea ice classification. One limitation for this article was that in the four model-based decomposition methods analyzed, relatively simple volume scattering models were utilized. These simple models are not intended to represent the full complexity of the scatterers forming the sea ice medium. Recently, improved volume scattering models considering the diploes' shape and orientation as well as dielectric constant properties have been proposed [21], [73], which hold great potential to achieve more reliable decomposed results. However, the use of these advanced volume scattering models would introduce more unknown parameters in the polarimetric decomposition and renders the polarimetric decomposition more sophisticated, which warrants further analysis. Meanwhile, only three polarimetric features were extracted from the decomposition techniques and used for sea ice classification. Previous studies have shown that elements of the measured coherency or covariance matrix can also be treated as features in the classifier and help to improve image classification accuracy by using deep learning algorithms [74], [75]. Future work includes testing the combination of different types of features in more advanced image classification algorithms.

Acknowledgment

The authors would like to thank the National Satellite Ocean Application Service for providing the GF-3 SAR data. The GF-3 data are available from the website of China Ocean Satellite Data Service Center,[1] after registering and ordering.

References

[1] M. C. Serreze and W. N. Meier, "The Arctic's sea ice cover: Trends, variability, predictability, and comparisons to the antarctic," *Ann. New York Acad. Sci.*, vol. 1436, no. 1, pp. 36–53, 2019.

[2] J. C. Stroeve, T. Markus, L. Boisvert, J. Miller, and A. Barrett, "Changes in arctic melt season and implications for sea ice loss," *Geophysical Res. Lett.*, vol. 41, no. 4, pp. 1216–1225, 2014.

[3] J. A. Curry, J. L. Schramm, and E. E. Ebert, "Sea Ice-albedo climate feedback mechanism," *J. Climate*, vol. 8, no. 2, pp. 240–247, 1995.

[4] S. R. Stephenson, L. C. Smith, L. W. Brigham, and J. A. Agnew, "Projected 21st-century changes to arctic marine access," *Climatic Change*, vol. 118, no. 3, pp. 885–899, 2013.

[5] S. Ochilov and D. A. Clausi, "Operational SAR sea-ice image classification," *IEEE Trans. Geosci. Remote Sens.*, vol. 50, no. 11, pp. 4397–4408, Nov. 2012.

[6] N. Y. Zakhvatkina, V. Y. Alexandrov, O. M. Johannessen, S. Sandven, and I. Y. Frolov, "Classification of sea ice types in ENVISAT synthetic aperture radar images," *IEEE Trans. Geosci. Remote Sens.*, vol. 51, no. 5, pp. 2587–2600, May 2013.

[7] R. Ressel, A. Frost, and S. Lehner, "A neural network-based classification for sea ice types on X-band SAR images," *IEEE J. Sel. Topics Appl. Earth Observ. Remote Sens.*, vol. 8, no. 7, pp. 3672–3680, Jul. 2015.

[8] H. Liu, H. Guo, and L. Zhang, "SVM-based sea ice classification using textural features and concentration from RADARSAT-2 dual-pol ScanSAR data," *IEEE J. Sel. Topics Appl. Earth Observ. Remote Sens.*, vol. 8, no. 4, pp. 1601–1613, Apr. 2015.

[9] J. W. Park, A. A. Korosov, M. Babiker, J. S. Won, M. W. Hansen, and H. C. Kim, "Classification of sea ice types in sentinel-1 synthetic aperture radar images," *Cryosphere*, vol. 14, no. 8, pp. 2629–2645, 2020.

[10] W. Song *et al.*, "Automatic sea-Ice classification of SAR images based on spatial and temporal features learning," *IEEE Trans. Geosci. Remote Sens.*, vol. 59, no. 12, pp. 9887–9901, Dec. 2021.

[11] T. Geldsetzer and J. J. Yackel, "Sea ice type and open water discrimination using dual co-polarized C-band SAR," *Can. J. Remote Sens.*, vol. 35, no. 1, pp. 73–84, 2009.

[12] M. Dabboor and T. Geldsetzer, "Towards sea ice classification using simulated RADARSAT constellation mission compact polarimetric SAR imagery," *Remote Sens. Environ.*, vol. 140, pp. 189–195, 2014.

[13] N. Zakhvatkina, V. Smirnov, and I. Bychkova, "Satellite SAR data-based sea ice classification: An overview," *Geosciences*, vol. 9, no. 4, pp. 152–166, 2019.

[14] H. Li and W. Perrie, "Sea ice characterization and classification using hybrid polarimetry SAR," *IEEE J. Sel. Topics Appl. Earth Observ. Remote Sens.*, vol. 9, no. 11, pp. 4998–5010, Nov. 2016.

[15] R. Ressel, S. Singha, S. Lehner, A. Rösel, and G. Spreen, "Investigation into different polarimetric features for sea ice classification using X-Band synthetic aperture radar," *IEEE J. Sel. Topics Appl. Earth Observ. Remote Sens.*, vol. 9, no. 7, pp. 3131–3143, Jul. 2016.

[16] L. K. Soh and C. Tsatsoulis, "Texture analysis of SAR sea ice imagery using gray level co-occurrence matrices," *IEEE Trans. Geosci. Remote Sens.*, vol. 37, no. 2, pp. 780–795, Mar. 1999.

[1] [Online]. Available: https://osdds.nsoas.org.cn/, accessed on April 8, 2021.

[17] I. Hajnsek, E. Pottier, and S. R. Cloude, "Inversion of surface parameters from polarimetric SAR," *IEEE Trans. Geosci. Remote Sens.*, vol. 41, no. 4, pp. 727–744, Apr. 2003.

[18] I. Hajnsek, T. Jagdhuber, H. Schon, and K. P. Papathanassiou, "Potential of estimating soil moisture under vegetation cover by means of PolSAR," *IEEE Trans. Geosci. Remote Sens.*, vol. 47, no. 2, pp. 442–454, Feb. 2009.

[19] L. He, R. Panciera, M. A. Tanase, J. P. Walker, and Q. Qin, "Soil moisture retrieval in agricultural fields using adaptive model-based polarimetric decomposition of SAR data," *IEEE Trans. Geosci. Remote Sens.*, vol. 54, no. 8, pp. 4445–4460, Aug. 2016.

[20] J. P. S. Gill, J. J. Yackel, T. Geldsetzer, and M. C. Fuller, "Sensitivity of C-band synthetic aperture radar polarimetric parameters to snow thickness over landfast smooth first-year sea ice," *Remote Sens. Environ.*, vol. 166, pp. 34–49, 2015.

[21] Z. Xi, W. Dierking, Z. Jie, and M. Junmin, "A polarimetric decomposition method for ice in the bohai sea using C-Band PolSAR data," *IEEE J. Sel. Topics Appl. Earth Observ. Remote Sens.*, vol. 8, no. 1, pp. 47–66, Jan. 2015.

[22] M. Shokr and M. Dabboor, "Observations of SAR polarimetric parameters of lake and fast sea ice during the early growth phase," *Remote Sens. Environ.*, vol. 247, 2020, Art. no. 111910.

[23] B. Scheuchl, I. Hajnsek, and I. G. Cumming, "Model-based classification of polarimetric SAR sea ice data," in *Proc. IEEE Int. Geosci. Remote Sens. Symp.*, 2002, pp. 1521–1523.

[24] A. Rodrigues, D. Corr, K. Partington, E. Pottier, and L. Ferro-Famil, "Unsupervised wishart classifications of sea-ice using entropy, alpha and anisotropy decompositions," *Appl. SAR Polarimetry Polarimetric Interferometry*, vol. 529, , 2003, Art. no. 17.1.

[25] B. Scheuchl, I. Cumming, and I. Hajnsek, "Classification of fully polarimetric single- and dual-frequency SAR data of sea ice using the wishart statistics," *Can. J. Remote Sens.*, vol. 31, no. 1, pp. 61–72, 2005.

[26] M. Hossain, J. Yackel, M. Dabboor, and M. C. Fuller, "Application of a three-component scattering model over snow-covered first-year sea ice using polarimetric C-band SAR data," *Int. J. Remote Sens.*, vol. 35, no. 5, pp. 1786–1803, 2014.

[27] J. P. S. Gill and J. J. Yackel, "Evaluation of C-band SAR polarimetric parameters for discrimination of first-year sea ice types," *Can. J. Remote Sens.*, vol. 38, no. 3, pp. 306–323, 2012.

[28] J. P. S. Gill, J. J. Yackel, and T. Geldsetzer, "Analysis of consistency in first-year sea ice classification potential of C-band SAR polarimetric parameters," *Can. J. Remote Sens.*, vol. 39, no. 2, pp. 101–117, 2013.

[29] S. Singha and R. Ressel, "Arctic sea ice characterization using RISAT-1 compact-pol SAR imagery and feature evaluation: A case study over northeast Greenland," *IEEE J. Sel. Topics Appl. Earth Observ. Remote Sens.*, vol. 10, no. 8, pp. 3504–3514, Aug. 2017.

[30] S. Singha, M. Johansson, N. Hughes, S. M. Hvidegaard, and H. Skourup, "Arctic sea ice characterization using spaceborne fully polarimetric L-, C-, and X-Band SAR with validation by airborne measurements," *IEEE Trans. Geosci. Remote Sens.*, vol. 56, no. 7, pp. 3715–3734, Jul. 2018.

[31] K. Warner, J. Iacozza, R. Scharien, and D. Barber, "On the classification of melt season first-year and multi-year sea ice in the beaufort sea using radarsat-2 data," *Int. J. Remote Sens.*, vol. 34, no. 11, pp. 3760–3774, 2013.

[32] T. Geldsetzer, M. Arkett, T. Zagon, F. Charbonneau, J. J. Yackel, and R. K. Scharien, "All-season compact-polarimetry C-band SAR observations of sea ice," *Can. J. Remote Sens.*, vol. 41, no. 5, pp. 485–504, 2015.

[33] A. S. Fors, C. Brekke, A. P. Doulgeris, T. Eltoft, A. H. H. Renner, and S. Gerland, "Late-summer sea ice segmentation with multi-polarisation SAR features in C and X band," *Cryosphere*, vol. 10, no. 1, pp. 401–415, 2016.

[34] A. S. Fors, C. Brekke, S. Gerland, A. P. Doulgeris, and J. F. Beckers, "Late summer arctic sea ice surface roughness signatures in C-band SAR data," *IEEE J. Sel. Topics Appl. Earth Observ. Remote Sens.*, vol. 9, no. 3, pp. 1199–1215, Mar. 2016.

[35] J. A. Casey, S. E. L. Howell, A. Tivy, and C. Haas, "Separability of sea ice types from wide swath C- and L-band synthetic aperture radar imagery acquired during the melt season," *Remote Sens. Environ.*, vol. 174, pp. 314–328, 2016.

[36] S. Nasonova, R. K. Scharien, T. Geldsetzer, S. E. L. Howell, and D. Power, "Optimal compact polarimetric parameters and texture features for discriminating sea ice types during winter and advanced melt," *Can. J. Remote Sens.*, vol. 44, no. 4, pp. 390–411, 2018.

[37] S. Singha, A. M. Johansson, and A. P. Doulgeris, "Robustness of SAR sea ice type classification across incidence angles and seasons at L-band," *IEEE Trans. Geosci. Remote Sens.*, vol. 59, no. 12, pp. 9941–9952, Dec. 2021.

[38] S. R. Cloude and E. Pottier, "An entropy based classification scheme for land applications of polarimetric SAR," *IEEE Trans. Geosci. Remote Sens.*, vol. 35, no. 1, pp. 68–78, 1997.

[39] J. J. Van Zyl, Y. Kim, and M. Arii, "Requirements for model-based polarimetric decompositions," in *Proc. IEEE Int. Geosci. Remote Sens. Symp.*, Boston, MA, USA, 2008, pp. 417–420.

[40] J. J. Van Zyl, M. Arii, and Y. Kim, "Model-based decomposition of polarimetric SAR covariance matrices constrained for nonnegative eigenvalues," *IEEE Trans. Geosci. Remote Sens.*, vol. 49, no. 9, pp. 3452–3459, Sep. 2011.

[41] D. Xiang, Y. Ban, and Y. Su, "Model-based decomposition with cross scattering for polarimetric SAR urban areas," *IEEE Geosci. Remote Sens. Lett.*, vol. 12, no. 12, pp. 2496–2500, Dec. 2015.

[42] D. Xiang, T. Tang, Y. Ban, Y. Su, and G. Kuang, "Unsupervised polarimetric SAR urban area classification based on model-based decomposition with cross scattering," *ISPRS J. Photogramm. Remote Sens.*, vol. 116, pp. 86–100, 2016.

[43] Y. Yamaguchi, T. Moriyama, M. Ishido, and H. Yamada, "Four-component scattering model for polarimetric SAR image decomposition," *IEEE Trans. Geosci. Remote Sens.*, vol. 43, no. 8, pp. 1699–1706, Aug. 2005.

[44] T. Zhang *et al.*, "Deep learning based sea ice classification with Gaofen-3 fully polarimetric SAR data," *Remote Sens.*, vol. 13, no. 8, pp. 1452–1473, 2021.

[45] L. Xu, H. Zhang, C. Wang, and Q. Fu, "Classification of chinese Gaofen-3 fully-polarimetric SAR images: Initial results," in *Proc. Prog. Electromagnetics Res. Symp.*, 2017, pp. 700–705.

[46] L. Zhang, Q. Meng, J. Zeng, X. Wei, and H. Shi, "Evaluation of Gaofen-3 C-Band SAR for soil moisture retrieval using different polarimetric decomposition models," *IEEE J. Sel. Topics Appl. Earth Observ. Remote Sens.*, vol. 14, pp. 5707–5719, May 2021.

[47] A. Freeman and S. L. Durden, "A three-component scattering model for polarimetric SAR data," *IEEE Trans. Geosci. Remote Sens.*, vol. 36, no. 3, pp. 963–973, Mar. 1998.

[48] L. H. Smedsrud, M. H. Halvorsen, J. C. Stroeve, R. Zhang, and K. Kloster, "Fram strait sea ice export variability and september arctic sea ice extent over the last 80 years," *Cryosphere*, vol. 11, no. 1, pp. 65–79, 2017.

[49] R. A. Shuchman *et al.*, "Remote sensing of the fram strait marginal ice zone," *Science*, vol. 236, no. 4800, pp. 429–431, 1987.

[50] Q. Zhang, "System design and key technologies of the GF-3 satellite," *Acta Geodaetica et Cartographica Sinica*, vol. 46, no. 3, pp. 269–277, 2017.

[51] L. Shi, L. Yang, L. Zhao, P. Li, J. Yang, and L. Zhang, "NESZ estimation and calibration for Gaofen-3 polarimetric products by the minimum noise envelope estimator," *IEEE Trans. Geosci. Remote Sens.*, vol. 59, no. 9, pp. 7517–7534, Sep. 2021.

[52] S. Shangguan, X. Qiu, K. Fu, B. Lei, and W. Hong, "GF-3 polarimetric data quality assessment based on automatic extraction of distributed targets," *IEEE J. Sel. Topics Appl. Earth Observ. Remote Sens.*, vol. 13, pp. 4282–4294, May 2020.

[53] Y. Chang, P. Li, J. Yang, J. Zhao, L. Zhao, and L. Shi, "Polarimetric calibration and quality assessment of the GF-3 satellite images," *Sensors*, vol. 18, no. 2, pp. 403–414, 2018.

[54] S. Jiang, X. Qiu, B. Han, and W. Hu, "A quality assessment method based on common distributed targets for GF-3 polarimetric SAR data," *Sensors*, vol. 18, no. 3, pp. 807–825, 2018.

[55] L. Shi, P. Li, J. Yang, H. Sun, L. Zhao, and L. Zhang, "Polarimetric calibration for the distributed Gaofen-3 product by an improved unitary zero helix framework," *ISPRS J. Photogramm. Remote Sens.*, vol. 160, pp. 229–243, 2020.

[56] J.-S. Lee, M. R. Grunes, and G. d. Grandi, "Polarimetric SAR speckle filtering and its implication for classification," *IEEE Trans. Geosci. Remote Sens.*, vol. 37, no. 5, pp. 2363–2373, May 1999.

[57] D. K. Hall and G. A. Riggs, *MODIS/Terra Sea Ice Extent Daily L3 Global 1km EASE-Grid Day, Version 61*. Boulder, CO, USA: National Snow & Ice Data Center, 2021.

[58] D. K. Hall, J. R. Key, K. A. Casey, G. A. Riggs, and D. J. Cavalieri, "Sea ice surface temperature product from MODIS," *IEEE Trans. Geosci. Remote Sens.*, vol. 42, no. 5, pp. 1076–1087, May 2004.

[59] R. Kwok, E. Rignot, B. Holt, and R. Onstott, "Identification of sea ice types in spaceborne synthetic aperture radar data," *J. Geophysical Res., Oceans*, vol. 97, no. C2, pp. 2391–2402, 1992.

[60] L. Breiman, "Random forests," *Mach. Learn.*, vol. 45, no. 1, pp. 5–32, 2001.

[61] M. Belgiu and L. Drăguţ, "Random forest in remote sensing: A review of applications and future directions," *ISPRS J. Photogramm. Remote Sens.*, vol. 114, pp. 24–31, 2016.

[62] F. Pedregosa *et al.*, "Scikit-learn: Machine learning in Python," *J. Mach. Learn. Res.*, vol. 12, pp. 2825–2830, 2011.
[63] S. V. Stehman, "Selecting and interpreting measures of thematic classification accuracy," *Remote Sens. Environ.*, vol. 62, no. 1, pp. 77–89, 1997.
[64] J. Cohen, "A coefficient of agreement for nominal scales," *Educ. Psychol. Meas.*, vol. 20, no. 1, pp. 37–46, 1960.
[65] M. Mäkynen and J. Karvonen, "Incidence angle dependence of first-year sea ice backscattering coefficient in sentinel-1 SAR imagery over the kara sea," *IEEE Trans. Geosci. Remote Sens.*, vol. 55, no. 11, pp. 6170–6181, Nov. 2017.
[66] M. S. Mahmud, T. Geldsetzer, S. E. L. Howell, J. J. Yackel, V. Nandan, and R. K. Scharien, "Incidence angle dependence of HH-Polarized C- and L-band wintertime backscatter over Arctic sea ice," *IEEE Trans. Geosci. Remote Sens.*, vol. 56, no. 11, pp. 6686–6698, Nov. 2018.
[67] W. Aldenhoff, L. E. B. Eriksson, Y. Ye, and C. Heuzé, "First-year and multiyear sea ice incidence angle normalization of dual-polarized sentinel-1 SAR images in the beaufort sea," *IEEE J. Sel. Topics Appl. Earth Observ. Remote Sens.*, vol. 13, pp. 1540–1550, Apr. 2020.
[68] J. Lohse, A. P. Doulgeris, and W. Dierking, "Mapping sea-ice types from sentinel-1 considering the surface-type dependent effect of incidence angle," *Ann. Glaciol.*, vol. 61, no. 83, pp. 260–270, 2020.
[69] J. Lohse, A. P. Doulgeris, and W. Dierking, "Incident angle dependence of sentinel-1 texture features for sea ice classification," *Remote Sens.*, vol. 13, no. 4, pp. 552–570, Feb. 2021.
[70] S. V. Nghiem *et al.*, "Evolution in polarimetric signatures of thin saline ice under constant growth," *Radio Sci.*, vol. 32, no. 1, pp. 127–151, 1997.
[71] H. Wakabayashi, T. Matsuoka, K. Nakamura, and F. Nishio, "Polarimetric characteristics of sea ice in the sea of okhotsk observed by airborne L-band SAR," *IEEE Trans. Geosci. Remote Sens.*, vol. 42, no. 11, pp. 2412–2425, 2004.
[72] A. Freeman, "An algorithm for estimating the noise levels in polarimetric SAR image data," *Int. J. Remote Sens.*, vol. 15, no. 9, pp. 1791–1798, 1994.
[73] G. Parrella, I. Hajnsek, and K. P. Papathanassiou, "Polarimetric decomposition of L-Band PolSAR backscattering over the austfonna ice cap," *IEEE Trans. Geosci. Remote Sens.*, vol. 54, no. 3, pp. 1267–1281, Mar. 2016.
[74] R. Shang, G. Wang, M. A. Okoth, and L. Jiao, "Complex-valued convolutional autoencoder and spatial pixel-squares refinement for polarimetric SAR image classification," *Remote Sens.*, vol. 11, no. 5, pp. 522–540, 2019.
[75] R. Shang, J. He, J. Wang, K. Xu, L. Jiao, and R. Stolkin, "Dense connection and depthwise separable convolution based CNN for polarimetric SAR image classification," *Knowl.-Based Syst.*, vol. 194, 2020, Art. no. 105542.

Lian He received the B.S. degree in remote sensing science and technology from Wuhan University, Wuhan, China, in 2010, and the Ph.D. degree in cartology and geography information system from Peking University, Beijing, China, in 2016.

From 2013 to 2014, he was a Visiting Research Student with the Department of Civil Engineering, Monash University, Melbourne, VIC, Australia. From 2016 to 2018, he was a Postdoctoral Fellow with the Department of Hydraulic Engineering, Tsinghua University, Beijing, China. Since 2020, he has been an Assistant Professor with the School of Geospatial Engineering and Science, Sun Yat-sen University, Zhuhai, China. His research interests include microwave remote sensing of soil moisture and sea ice change monitoring in Polar Regions.

Xiyi He received the B.S. degree in geographic information science from Changan University, Xi'an, China, in 2020. She is currently working toward the master's degree in resources and environment with the School of Geospatial Engineering and Science, Sun Yat-sen University, Zhuhai, China.

Her research interests include microwave remote sensing and sea ice classification.

Fengming Hui received the M.S. degree in geography from Liaocheng Teachers University, Liaocheng, China, in 2001, and the Ph.D. degree in cartography and geography information system from Nanjing University, Nanjing, China, in 2007.

He is currently a Professor with the School of Geospatial Engineering and Science, Sun Yat-sen University, Zhuhai, China. He has authored more than 30 articles. His research interest includes on mapping physical parameters of snow and ice in polar regions using remote sensing data and polar sea ice dynamics changes.

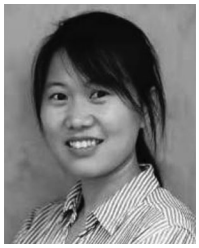

Yufang Ye received the B.S. degree in physics and the M.S. degree in remote sensing from Beijing Normal University, Beijing, China, in 2008 and 2011, respectively, the Ph.D. degree in environmental physics from the University of Bremen, Bremen, Germany, in 2016.

Between 2016 and 2017, she was with the group of "Remote Sensing of Polar Regions" in the Institute of Environmental Physics, University of Bremen, Bremen, Germany, working on sea ice monitoring with microwave remote sensing data. From 2017 to 2019, she was with the Radar and Optical Remote Sensing Division, Department of Space, Earth and Environment, Chalmers University of Technology, Gothenburg, Sweden, where she was working with RADAR remote sensing for ocean and sea ice applications. Since 2020, she has been holding a position as an Assistant Professor with the School of Geospatial Engineering and Science, Sun Yat-sen University, Guangzhou, China. Her research interests include remote sensing of polar regions with focus on monitoring sea ice changes (concentration, type, thickness, and dynamics) and understanding the mechanisms behind.

Tianyu Zhang received the M.S. degree in geomatics engineering from the Aerospace Information Research Institute, Chinese Academy of Sciences, Beijing, China, in 2019. She is currently working toward the Ph.D. degree in global environmental change with the College of Global Change and Earth System Science, Beijing Normal University, Beijing, China.

Her research interest includes in Arctic sea ice remote sensing.

Xiao Cheng received the B.E. degree in surveying engineering from Wuhan Technical University of Surveying and Mapping, Wuhan, China, in 1998, the M.S. degree in geodesy and measurement engineering from Wuhan University, Wuhan, China, in 2001, and the Ph.D. degree in cartography and geographic information systems from Chinese Academy Sciences, Beijing, China, in 2004.

In 2004, he was with the Institute of Remote Sensing Applications, Chinese Academy of Sciences, as an Assistant Researcher, and in 2008 became an Associate Researcher. In 2009, he moved to Beijing Normal University and is the Associate Dean with the College of Global Change and Earth System Science (GCESS), and became a Professor. In 2016, he was the Dean with the GCESS. In 2019, he was with Sun Yat-sen University, initiated the School of Geospatial Engineering and Science and act as the Dean. He has authored and coauthored more than 100 peer-reviewed journal papers, including one in PNAS in 2015. His current research interests include polar remote sensing technology and climate change in polar regions.

Dr. Cheng was the recipient of the award for Advanced Individual of China's Polar Exploration in 2017.